Chapter 5

Real-time optical plasma boundary reconstruction for plasma position control at the TCV Tokamak

5.1 Introduction

5.1.1 Plasma boundary reconstruction

In nuclear fusion plasmas, the plasma position and shape are often inferred from magnetic measurements and provided to a real-time control system for shape and position control [16][47][48]. Although this method is used on virtually all tokamaks, there are situations in which applicability of the magnetic sensing is limited [17]. Long plasma discharges can suffer from drift of the magnetic signals due to the integral nature of these measurements [18]. Similarly, plasmas with a low plasma current and large distance to the magnetic pick-up coils (for example during the ramp-up and ramp-down phase of the discharge or ITER first plasma [49]) may result in weak magnetic signals. For these reasons, alternative sensors have been proposed for measuring the plasma boundary such as reflectometer arrays [21].

In this work, an optical plasma boundary diagnostic for the TCV tokamak is presented to measure the plasma shape in real-time, adopting the OFIT approach presented in [23]. Such an optical measurement of the plasma boundary can provide a direct and absolute measurement, not susceptible to drifts during long experiments. Previously, real-time optical plasma edge detection in the midplane of the MAST tokamak was applied for position control [22], using an inversion of a linear camera image. The OFIT technique allows realtime global determination of the plasma boundary shape from 2 dimensional camera images by deriving the plasma boundary location from localized edge features without resorting to time-consuming tomographic inversion. The purpose of this paper is to present an example of an optical plasma boundary reconstruction in a real-time control environment, and to discuss on the basis of the experience gained, its merits in various control applications.

The paper is organized as follows: a short introduction to the RT-OFIT method is presented in the rest of this section. In Section 5.2, a design study is presented for the application of an OFIT diagnostic on the TCV tokamak for a single plasma configuration, resulting in a list of specifications for the diagnostic. In Section 5.3, we describe the development and implementation of the diagnostic according to these specifications. In Section 5.4, results of real-time plasma boundary reconstructions produced by the implemented diagnostic are presented, and the effect of narrowband optical filtering is shown and discussed. In Section 5.5, a real-time feedback control experiment of the plasma position is presented, using the RT-OFIT setup to measure the plasma position at a nominal acquisition and processing rate of 1000 frames per second.

This chapter has been published in: *Nuclear Fusion* **54** 073018 (2014) [24]

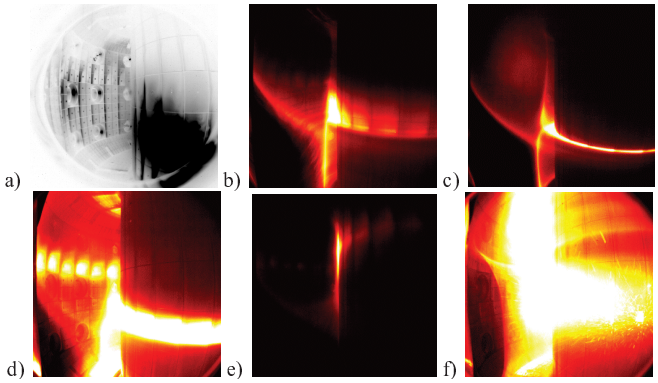

Figure 5.1: Examples of camera images of vacuum vessel and plasmas in the Tokamak Configuration Variable (TCV) [50]. Monochrome images are depicted in hot false color map. a) Illuminated inner vessel. The central column of the tokamak is in the right-half of the image and the outer vessel wall appears in the left-half of the image b) plasma boundary and strike point of a diverted plasma in L-mode c) plasma boundary and core radiation in an H-mode plasma d) intense radiation and wall reflections during an ELM e) a limited discharge f) plasma disruption with sparks.

5.1.2 Real-time optical plasma boundary diagnostic: RT-OFIT

Visible wavelength camera images of tokamak plasmas are typically dominated by Balmer deuterium-Alpha emission from unconfined neutral atoms, in the external region of the plasma. When reaching the plasma boundary, neutral deuterium atoms are excited by collisions with energetic plasma particles, and their consequent decay emits light in the visible range. Inside the plasma boundary, all particles are quickly ionized and the neutral density quickly diminishes. The light emitted by neutral particles is therefore expected to peak close to the plasma boundary.

Figure 5.1 shows a number of the phenomena that can be observed in the high resolution, high frame-rate tangential view camera images acquired with the RT-OFIT diagnostic. Figure 5.1 b and c show images of diverted plasmas that are dominated by strong plasma boundary features. Figure 5.1 a, d, e and f provide the same tangential view, but show that other phenomena may also be observed in camera images of tokamak plasmas during the course of the experiment. Figure 5.1 e shows a camera image of a plasma in limiter configuration. The light emission of such plasmas can be dominated by the interaction with the vessel-wall in the limiter region, and clearly resolvable plasma boundary features are not always produced.

The diagnostic uses the OFIT interpretation on the tangential view camera images presented in [23] to interpret the plasma boundary features of these visible images and provide a plasma shape measurement. The intensity of a pixel in the camera image represents the line-integrated light emission from a chord traversing the plasma volume. Assuming a thin emissive-shell model of the emission in the plasma boundary and toroidal symmetry of the plasma emission, the pixel intensity in tangential view images will peak for sightlines that are tangential to the plasma boundary. Figure 5.1 b and c show segments of the plasma boundaries clearly resolved as lines of peak intensity with strong and localized gradients in the direction normal to the boundary. These plasma boundary features in the image-plane can be transformed to the plasma boundary in the poloidal plane using the OFIT-transform. This approach avoids the complexity of tomographic inversions, making it suitable for real-time applications. The positions of the strike-points that radiate strongly from the wall of the vacuum vessel can also be extracted from the images to provide additional information on the plasma boundary shape. The real-time diagnostic can provide a number of key signals for use in plasma shape control, as well as providing new constraint for magnetic reconstruction codes [30, 51–54]. Additionally, the diagnostic can provide routine visible light surveillance of plasma discharges.

5.2 TCV tokamak camera positioning and control timescales

5.2.1 Camera positioning and reconstruction range

The Tokamak Configuration Variable (TCV) [50] is a medium sized tokamak operated at the CRPP Lausanne [55]. TCV was designed specifically to explore various plasma shapes to study their effect on plasma physics and confinement. Its highly elongated vacuum vessel with 16 regularly spaced poloidal field coils allows a multitude of plasma configurations. Three tangential ports are available in the vacuum vessel to provide a view of the plasma boundary suitable for optical plasma boundary reconstructions. These ports are located at the same toroidal segment of the machine at heights of $Z = -0.45$ m, $Z = 0$ m and $Z = 0.45$ m for the upper, midplane and lower ports respectively. The views provided by these ports determine the reconstruction range for OFIT given by the visibility condition presented in [23]:

$$\sqrt{u_c^2 + w_c^2} = R_c \geq |R_e - (Z_e - v_c)\frac{dR_e}{dZ_e}|, \tag{5.1}$$

where (u_c, v_c, w_c) is the effective pinhole location of the light collecting optics in coordinates as shown in Figure 2.3, through which all observational chords pass, and $(R_e, Z_e, dR_e/dZ_e)$ is a plasma edge coordinate in the poloidal plane and its local orientation in the poloidal plane dR/dZ. When this visibility condition is satisfied, a sightline exists from the pinhole of the light collection optics, tangential to the plasma boundary at $(R_e, Z_e, dR_e/dZ_e)$. Intuitively, the visibility condition can be visualized by a cone fitting around the three dimensional plasma boundary at $C_e = (R_e, Z_e, dR_e/dZ_e)$, where C_e represents an infinitesimal conical section of the plasma boundary. For a tangential sightline from the camera to the point C_e to exist, the camera must be located outside this cone. An additional requirement is that this sightline is within the view of the camera and not obstructed by other structures between the pinhole point of the optics and the plasma boundary.

The work in this paper is restricted to the analysis and reconstruction of plasma discharges of a single configuration, the TCV standard shot; an L-mode single null diverted discharge centered at $z = 0.23$ m, run at the start of every operational day for calibration purposes. Such discharges last for 2 seconds and have approximately a 1.5 s flattop with stable plasma conditions. The diverted plasma configuration with an appreciable distance between the plasma boundary and the first wall results in well defined boundary features in the camera images, with little polluting light from reflections or plasma-wall interaction in the regions of interest. In Figure 2, the visibility criterion of eq. (5.1) is applied to standard shot plasma boundary shape. For three different camera locations (u_c, v_c, w_c), corresponding to the three tangential ports, synthesized camera images are shown and the corresponding reconstruction range of the plasma boundary from the port is given. This analysis is based on an 80 degree angle of view from behind the window of the port plug. A two-camera setup was chosen for sufficient coverage of the plasma boundary of the standard shot, with one camera placed on the mid-plane as well as the upper port.

5.2.2 Feedback control timescales

The RT-OFIT diagnostic has to provide accurate real-time measurements of the visible plasma boundary segments from two cameras. To be used for real-time plasma shape control, the response time, or measurement delay of the diagnostic is crucial. The performance of a feedback control system is commonly expressed as its control bandwidth f_{bw}; the frequency up to which disturbances can be rejected and reference signals can be tracked. This frequency corresponds to the *cross-over frequency* of the open loop transfer function, defined as the frequency where the gain is exactly 1 (0dB). For stability of the control loop, the total phase lag of the open loop transfer function may not exceed 180 degrees at the cross-over frequency. Typically, loop dynamics, including plant and actuator behavior and control algorithms, account for 90 degrees or more phase lag, and 30-60 degree stability margins are adopted for robustness [56]. This imposes strict requirements on the delay of the measurement system used in the feedback loop. The effective delay of a discrete time measurement system depends on the sampling rate and the processing time according to:

$$\Delta t_m = \frac{1}{2f_s} + \Delta t_{proc} + \Delta t_{obs}, \tag{5.2}$$

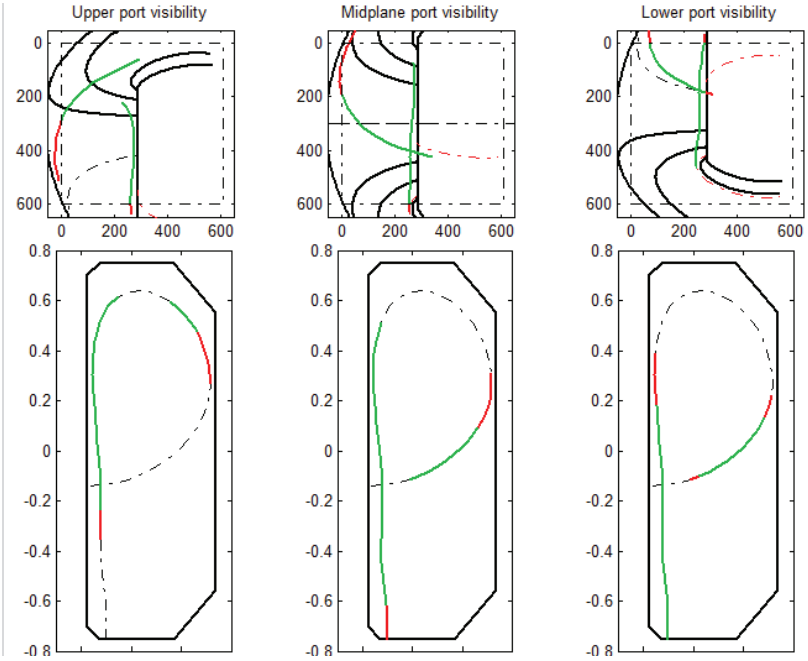

Figure 5.2: Plasma boundary visibility analysis for TCV standard shot. Upper diagrams show synthesized camera images, with the vacuum vessel drawn in black, and the expected boundary features in green and red. Strike locations on the central column and machine floor are also drawn as red dash-dotted lines. The black-dash-dot frame indicates the limits of view of the imaging system. As the tangential ports on TCV are oriented left of the central column, the right half of the pictures show the central column and the left half the outer vessel wall. As a consequence of the wide angle optics, the images have significant radial barreling distortion. This results in a curved outer vessel wall. Lower plots show machine cross-sections, with the full plasma boundary drawn in dash-dotted black and the visible segments for the corresponding ports drawn in blue. Red segments indicate parts of the plasma boundary that satisfy equation 5.1, but are outside the view of the camera system.

where Δt_m is the effective measurement delay, f_s is the sampling rate of the measurement, Δt_{obs} is the observation time required to obtain a measurement and Δt_{proc} is the processing time between the physical observation and the output of the measurement variable. The effective measurement delay has the effect of a phase delay $\Delta\phi_m = \Delta t_m \cdot f_{bw} \cdot 360$ at the control bandwidth. In TCV, the plasma position and shape respond to requests in poloidal field coil currents with a timescale of 10 ms, presenting an upper limit for the achievable control bandwidth. Control systems typically operate with a sampling rate one order of magnitude above the control bandwidth, hence, a sampling rate of 1000 Hz was chosen, while minimizing processing delay of the reconstruction output, which is expected to be 1-2 ms.

To acquire useful plasma images, the intensity of the images must be within the dynamic range of the camera. The intensity of the light emitted by the plasma between and even during shots is greatly varying, usually exceeding the dynamic range of available cameras. Camera exposure control is required to prevent saturation of the images in the various stages of the discharge. The cameras used require magnetic shielding for operation during plasma discharges. The space required for an effective shielding solution has consequences for the positioning of the camera and therefore the design of the optics.

5.3 RT-OFIT system design and implementation

The RT-OFIT setup consists of two relay optics, two real-time cameras and an acquisition and processing PC. The relay optics project a wide-angle view obtained at the tangential port windows to the detector chips of the cameras, placed behind the ports. The PC incorporates two Silicon Software framegrabbers with onboard Field Programmable Gate Array (FPGA) processors [57]; acquisition and processing boards that communicate with the cameras via a dedicated CameraLink interface [58]. In the following paragraphs the design and functionality of the optics, cameras and acquisition and processing PC are presented, and finally the parameters of the boundary reconstruction are discussed briefly.

5.3.1 Optics

Three tangential ports are available in the vacuum vessel to provide a view of the plasma boundary suitable for optical plasma boundary reconstructions. From these ports, a wide-angle view is desired for maximum reconstruction range. A common wide-angle objective could provide such a view when placed at the window of the tangential port. However, this would imply a camera location inside the port plug, where the limited available space inhibits an effective magnetic shielding solution. Additionally, the confined space inside the port plug makes handling of the camera unpractical and higher radiation levels and magnetic and electric field strengths are expected. By using a relay optic to relay the wide angle view obtained at the port window to a location behind the tangential port, the cameras can be placed within practical reach and a magnetic shielding solution is possible. The magnetic shields are supported by a separate structure from the cameras, to isolate mechanical forces on the shields from the imaging system.

The relay optics are constructed from standardized Thorlabs components [59]. A standard objective is used as a final, adjustable focusing element with adjustable aperture. The optics have a total length of 62 cm and project the 86 degree angle of view at the port window onto a spot of 12 mm radius on the camera detector chip, which has a size of 17.92x14.34 mm.

Cameras sensitive in the visible spectrum are used. One of the relay-optics allows for the use of wavelength filters. Filters can be inserted in a slit in the optics tube at the position where the light rays are most parallel. The maximum angle of light rays in this position is 4 degrees from the axis of the optic, which is accommodated by the applied filters. Such filters may be fitted to observe only emission of selected wavelength. This can however significantly reduce the light intensity available for imaging. Additionally, broadband visible light images are expected to be dominated by deuterium-Alpha emission from excited neutral species, whereas selected emission lines may originate from confined ionized species inside the plasma boundary, which may result in a shift of the detected boundary features. Figure 5.3 shows a Zemax drawing of the optics and a picture of the finalized optics, objective and camera. Figure 5.4 shows how the imaging setup is installed on the TCV tangential port.

The text on feedback control stability has been rephrased compared to [24] to more correctly convey the requirements for closed loop stability.

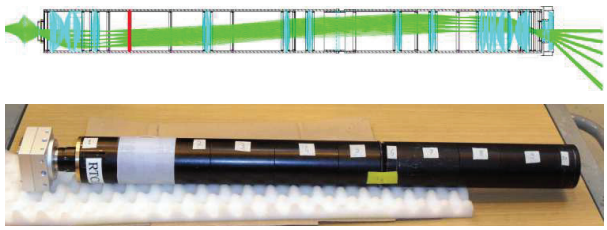

Figure 5.3: (top) Zemax drawing of relay optic, showing tubes, lenses and light rays. Light enters the optic on the right, and travels towards the camera on the left end of the optic. The red line shows where a narrowband interference filter may be inserted. (bottom) finalized optics and camera. The camera is shown on the left side of the relay optic, mounted to the final focusing objective.

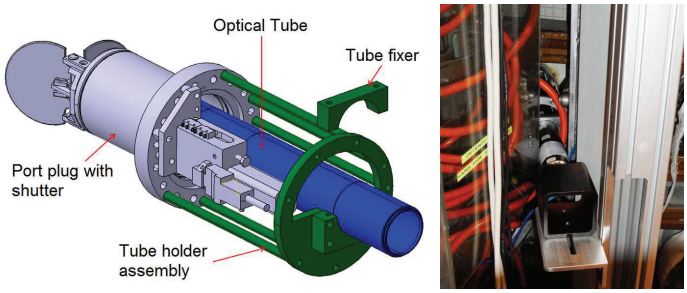

Figure 5.4: (left) CAD drawing of tangential port plug, optic and support structure. (right) Optic installed on the TCV mid-plane tangential port. Also showing magnetic shielding required for reliable operation of the cameras during discharges.

5.3.2 Cameras

The two cameras used (Optronis CL600X2 models [60] which apply 1280x1024 pixel, 17.92x14.34 mm monochrome CMOS sensors) can acquire and transmit 506 frames per second at full resolution, or more at reduced image size. In this application, a 608x600 pixel image size, corresponding to an 8.5x8.5 mm area on the sensor, was used at a nominal frame-rate of 1000 frames per second. The dynamic range of the ADC circuits on the cameras is 10 bits. Via lookup-tables, this data is mapped onto an 8 bits range, which reduces the intensity resolution but not the dynamic range, as the minimum and maximum light intensity that can be discerned remains unchanged, while the discretization steps are increased. The cameras generate frames of 356 kB per image at a 1000 Hz frame-rate from two cameras resulting in an effective bandwidth of 700 MB/s to the acquisition and processing PC.

5.3.3 Acquisition and Processing

The acquisition and processing PC handles camera control, image acquisition, synchronization with the TCV shot cycle, extraction of the plasma boundary information from the raw image data and transmission of optically reconstructed shape parameters to the plasma control system.

The 700 MB/s of data from the cameras is transferred to the framegrabbers via CameraLink interface. In the applied configuration, this interface has a maximum bandwidth of 503 MB/s per camera. Thus, the acquisition of a single image from camera to framegrabber takes 690 μs. The images acquired by the cameras must be transferred and processed quickly to provide output signals with minimal delay to maximize control bandwidth. In view of the large datasets per image it is critical to minimize data transfers and to use optimized processing techniques to minimize the response time of the diagnostic.

The processing required to reconstruct the shape of the plasma boundary from the camera images can be split up into an image processing step, that extracts the boundary features from the image, and a coordinate transformation step, that translates the boundaries coordinates in the image into boundaries in the poloidal plane. To prevent additional time consuming data transfers, the images are processed directly on the FPGAs of the framegrabber. An FPGA can be seen as a large switchboard of reconfigurable logic

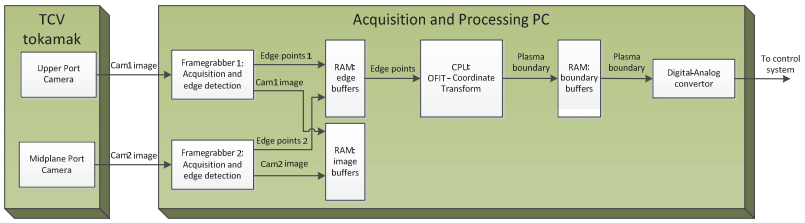

Figure 5.5: Schematic of processing steps and data-flow in RT-OFIT setup, from camera to signal output.

blocks, which is loaded with a hardware implementation to perform custom functionality in hardware. Once loaded with a hardware implementation, an FPGA effectively behaves as if it were an Application Specific Integrated Circuit (ASIC). Using this method, a custom hardware implementation was developed to handle boundary detection on the raw image data in the FPGA, executing the image processing with a high degree of parallelism and no software overhead, resulting in very short and deterministic processing times. This processing step provides the coordinates of the detected boundary features in the image, and results in a drastic reduction in data size compared with the raw images. The boundary coordinates are then sent over PCI express bus to the host RAM, and the OFIT-transform and further post-processing is handled in software by the CPU. Raw-image data is also recorded for visual inspection and post-shot analysis. The time between closing of the camera-shutters and output of the boundary coordinates from the framegrabbers was measured to be 880 μs. The measured delay to the finished reconstruction output was 1050 μs.

Real-time adaptive shutter logic is applied to optimize the intensity of the images within the available 10 bits dynamic range of the camera. This logic is implemented in the FPGA of a Silicon Software framegrabber. The exposure time for frame N+2 is updated on the basis of frame N, by calculating the average image intensity of a selected part of the image and adapting the exposure time to obtain the desired average image intensity. The exposure time for every frame is stored for post-shot analysis.

The software architecture is based on a real-time linux environment running a real-time application built using MATLAB Simulink Coder. This provides a high-level graphical programming environment that allows rapid development and prototyping by wrapping C-code functionally in the Simulink framework in a so-called S-function format. The framegrabber interface is also integrated as an S-function block in the Simulink model structure, which communicates with the framegrabbers drivers and also triggers the execution of a single time-step of the reconstruction upon the arrival of a new frame.

For feedback control experiments, a simplified integration into the TCV plasma control system was chosen by transmitting output signals across up to four analog channels to the plasma control system. This avoids timing and synchronization issues between diagnostic and control setup, and provides sufficient functionality for a proof-of-concept feedback control experiment. The control system samples and processes incoming analog signals at a rate of 10 kHz, thus the extra delay introduced in this step is less than 0.1 ms.

Figure 5.5 gives an overview of the dataflow in the RT-OFIT system, showing data transfers, processing steps and buffers.

5.3.4 Boundary Reconstruction parameters

To extract the plasma boundary features from the camera images and to transform them to the plasma boundary in the poloidal plane, a number of reconstruction parameters must be set.

In each camera image, a set of Regions of Interest (ROI) is defined where the boundary features are sought. Each ROI covers a region of the image where a single segment of plasma boundary is expected. These regions of interest have the shape of curved-rectangles that encompass the expected location of the plasma boundary features. In the resampled sub-images, the feature detection algorithm seeks the maximum gradient in radial direction to determine the location of the plasma boundary. The detected boundary feature is then transformed to the poloidal plane using the OFIT-transform.

Currently, ROIs are set manually, and are specific to a certain plasma boundary shape. Automated ROI generation and/or ROI parameter updates during the discharge are conceivable to improve the automation of the method, but have not yet been implemented. Figure 5.6 shows the ROIs for a standard, single null

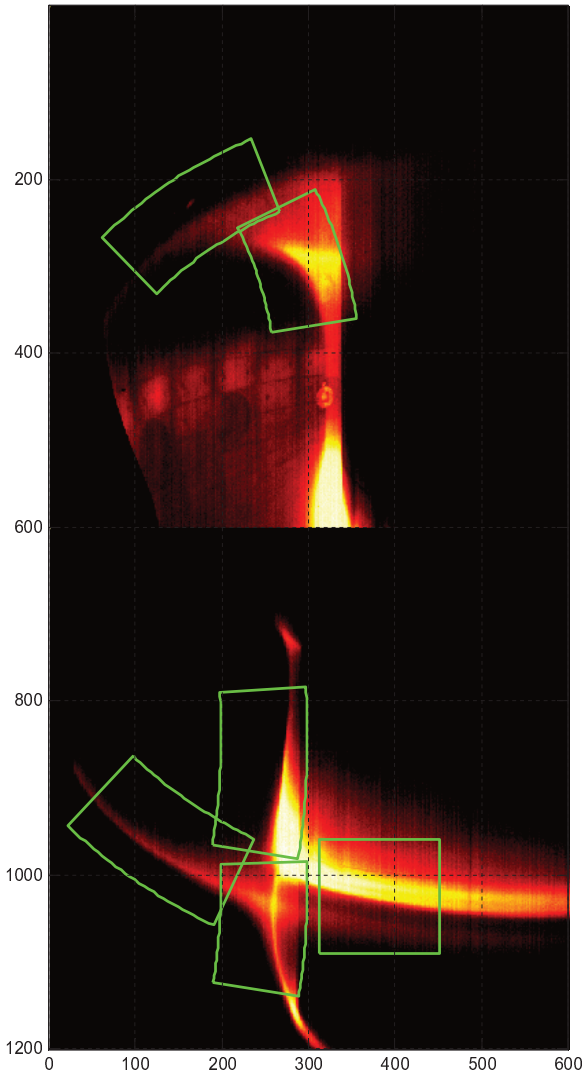

Figure 5.6: Regions of Interest (in green) need to be positioned to enclose the plasma boundary in the image. Shown are the chosen ROIs for the TCV standard shot in images from upper-port (top) and mid-plane port (bottom) cameras.

diverted plasma. Also shown is the ROI for the detection of the inner strike-point, which also covers an edge-feature in the camera images but has a different interpretation than the plasma boundary segments.

The boundary detection algorithm provides, for each ROI, a line segment in the image plane. To transform this into a plasma boundary segment in the poloidal plane using the OFIT-transform, a camera model is required that, for each pixel in the image, defines the trajectory of the corresponding sightlines in tokamak coordinates.

A pinhole camera model with a 2^{nd} order radial distortion is used to define the projection properties [23]. The pinhole model is parameterized by a pinhole location in tokamak coordinates, the direction of the optical axis, a magnification factor and radial distortion coefficients. The parameters are calibrated manually for both cameras by minimizing the distance between the observed and predicted pixel coordinates of a number of tokamak structures that are identified in the image, resulting in a static mapping of pixels to sightlines.

5.4 RT-OFIT Reconstruction results

Since the installation of the RT-OFIT setup, all plasma discharges were recorded and stored for visual observation and analysis. Figure 5.6 shows the TCV standard-shot shape and the camera images from this plasma configuration during the current-flattop, where the plasma shape and most other plasma parameters are constant. First results are presented for this plasma configuration.

The images shown in Figure 5.6 were processed in real-time by the RT-OFIT setup. An example reconstruction of shot 48858 is shown in Figure 5.7 a. In this frame, boundary signals are visible in all ROIs, providing 5 optically reconstructed boundary segments and one strike point location. The flux map and plasma boundary as determined by the LIUQE equilibrium reconstruction code [54] are shown for comparison. The reconstructed boundary segments are in close agreement with equilibrium reconstruction, typically within 1cm when a well resolved boundary feature is present in the camera images.

The obtained reconstruction range is close to the predicted range shown in Figure 5.2. Around the x-point, a smaller Region of Interest was chosen for the horizontal boundary segment. In this region, the visibility condition of equation (5.1) is only marginally satisfied due to the almost-horizontal surface orientation, resulting in a lower contrast of the pixels around the plasma boundary. Additionally, this part of the boundary segment appears in the same part of the camera image where the bright lower diverted leg is visible, resulting in overlapping boundary features that further impede a robust detection of the boundary feature. On the low field side (far left part of the camera images) the reconstruction range of the boundary segment is slightly reduced due to port and vessel structures that obstruct the view of the plasma.

In the example shown in Figure 5.7 a, the plasma boundary is visible in all Regions of Interest. However, during the flattop interval of such shots, the visibility of the plasma boundary in the upper half of the plasma boundary was poor and variable. In such cases, only the lower segments of plasma boundary can be reconstructed. This is depicted in Figure 5.7 b. Various modifications to the plasma discharge were attempted to obtain a reliable, poloidally homogeneous emission profile, but a suitable plasma configuration was not found. The poloidal emission profile of visible light of the plasma was experimentally observed to depend strongly on the recycling regime. Limiter regions or strike points are a strong source of neutral deuterium, the atom responsible for the majority of light emission. In the poloidal vicinity of these recycling regions, neutral deuterium concentration is high, and at the plasma boundary significant light emission from excited atoms is expected. From these images, it is concluded that the neutral particles are not distributed evenly around the plasma during the discharge, resulting in the observed inhomogenity. Experiments confirmed that a plasma configuration with an upper-null divertor produces light emission from the plasma boundaries in the top half of the plasma, but not in the bottom half. Deuterium fuelling, the other source of neutral deuterium, was found to have minimal effect on the poloidal emission profile, as it has a smaller contribution to the neutral influx in the machine than the recycling regions at the walls.

In H-mode plasma discharges with ELMs [61], the edge gradients of electron temperature T_e and density n_e are increased. This results in a narrower light emitting band in the boundary regions in inter-ELM phases, as shown in Figure 5.7 c, but inhibited useful reconstructions during ELMs. At the 1000 Hz frame rate, each ELM affects only one frame. Additionally, core emission from Brehmsstrahlung due to high core density was observed, associated with the H-mode density build-up, normally terminating in a disruption,

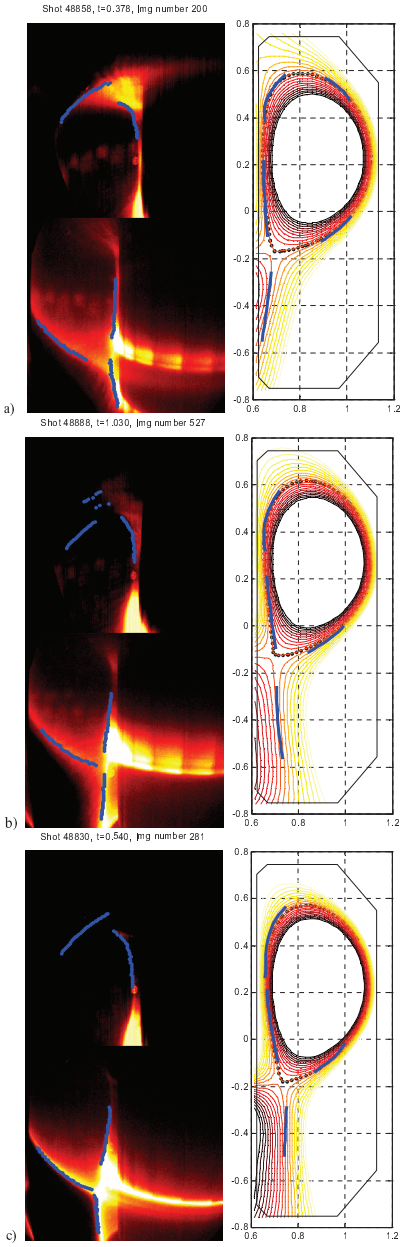

Figure 5.7: Camera images and optical boundary reconstruction: a) shot 48858, at the end of the ramp-up phase. Optically reconstructed segments are drawn blue. Magnetic reconstruction of last closed flux surface (black dots) and adjacent flux surfaces (coloured lines) in the poloidal plane are also shown for comparison. b) shot 48888 during flattop. The visibility of the upper-outer half of the plasma boundary is lost, c) diverted H-mode shot 48830, showing increased contrast and localization of boundary features.

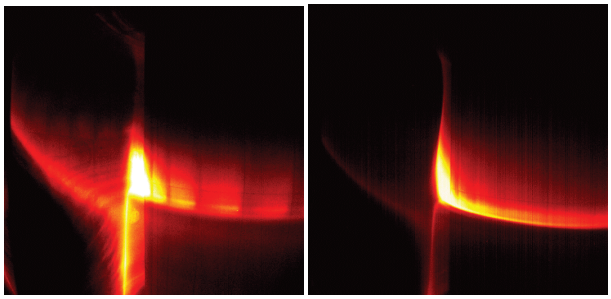

Figure 5.8: Visible wavelength (left) and C-III line emission (right) images of a standard shot at the start of flattop. A longer exposure time and larger aperture setting were used to obtain C-III-filtered images of similar intensity.

as shown in Figure 5.1 c (Bremsstrahlung) and f (disruption). The optical boundary reconstruction was, however, not directly affected by the Brehmsstrahlung as long as the plasma boundary features retained sufficient contrast.

The reconstruction results shown so far have been obtained using unfiltered, broad wavelength visible light images. If an emission line is present of a confined ion species that is active at the temperatures of the plasma boundary, the use of a wavelength filter could result in more localized boundary features in the image. This can improve signal to noise of the boundary measurement by preferentially rejecting polluting light sources not originating from the plasma boundary. As the emission comes from confined particles, their emission may also more accurately depict the shape of local flux surfaces. To test this, a 466 nm filter was inserted in the optical path, to obtain images of the Carbon-III emission line, which is typically strong in tokamaks with carbon walls such as TCV and emits close to the plasma boundary.

Figure 5.8 shows a comparison of camera images taken of a standard shot at the start of flattop, with and without the C-III filter installed. Both images display plasma boundary and strike point features, but in the C-III image the features are more localized, the filamentary scrape-off layer structures in the visible images are not present, and fewer reflections from the machine walls are visible. In Figure 5.9, a comparison is shown of an OFIT lower-boundary measurement using visible wavelength and C-III filtered images. The lower boundary is defined as the position of the lower plasma boundary at a radius of R=0.9 m. The uncertainty in the localization of the lower plasma boundary in the signal obtained using C-III filtered images is significantly reduced. The effective spatial resolution of the camera images at the outer plasma boundary is 1 mm, the mean amplitude of uncertainty in the boundary measurement is estimated at 5 mm when using broadband visible images, and 2 mm using C-III filtered images. Because these signals were obtained from two separate experiments, the absolute position of both signals should therefore not be directly compared.

This experiment demonstrates that emission from a confined ion species can also produce localized plasma boundary features, suitable for reconstruction with the OFIT method. Provided that a suitably radiating impurity is present in the plasma, OFIT can also be used also on high temperature machines where less visible light emission from neutral species is expected. In this particular example, the reconstruction results are actually improved by observing emission from a confined ion species, versus broadband emission predominantly from unconfined gasses. In the following chapter, all data is obtained from C-III filtered images.

A situation in which optical boundary reconstruction could provide unique information is during the ramp-up and -down phases of a discharge, where there is low plasma current and a large distance between magnetic pick-up sensors and the plasma current, resulting in weak signals for reconstruction. Additionally, the significant gap between plasma column and vessel wall allows for a more favorable relative position of the plasma boundary to the viewpoint of a camera, and therefore a larger visible fraction of the plasma boundary. Figure 10 shows a camera image during the ramp-down of a standard shot, where the plasma has evolved to a circular shape of reduced size.

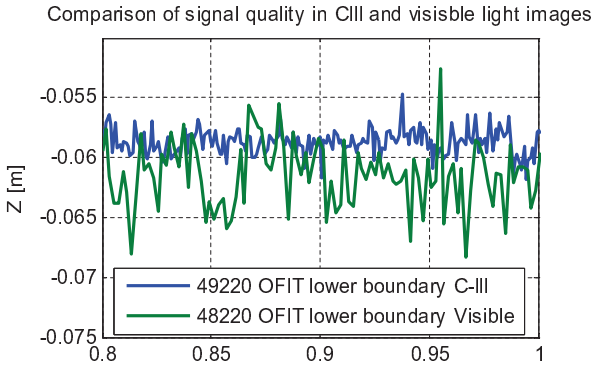

Figure 5.9: Comparison of OFIT lower-boundary signal using broadband visible or CIII line emission images.

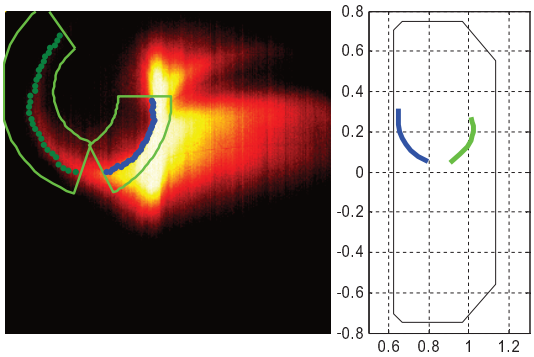

Figure 5.10: Mid-plane camera image and optical boundary reconstruction during ramp-down of standard shot.

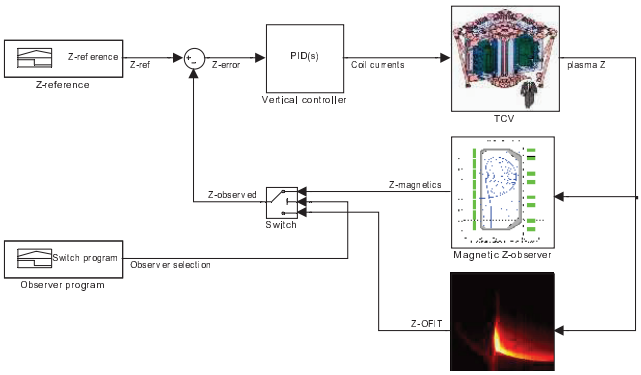

Figure 5.11: Feedback scheme for OFIT feedback control experiments.

5.5 Feedback control experiments

To demonstrate the real-time properties of the OFIT setup, a feedback control experiment was set up where the vertical position of the plasma was controlled using the optically reconstructed plasma boundary.

Elongated plasmas such as the TCV standard discharge are vertically unstable. In TCV, a fast-vertical controller is used to slow down the vertical instability of elongated plasmas by producing a negative feedback to the vertical velocity of the plasma, which is estimated using pickup-coils inside the vacuum vessel, and manipulated through fields generated by fast coils inside the vacuum chamber. Because the fast vertical controller provides feedback only on vertical velocity but not vertical position, the resulting vertical behavior of the plasma is still vertically unstable, but with a significantly slower growth rate. A slower timescale proportional-derivative controller is used to stabilize the remaining instability and to control the plasma vertical position using the external poloidal field coils. This vertical position controller feeds back on a vertical position Z observer, which is a function of the location and distribution of the plasma current, estimated using pick-up coils. In the control experiments presented here, the measurement of the vertical position of the plasma, normally provided by magnetic measurements at a rate of 10 kHz, was temporarily substituted by a measurement of the vertical position using the OFIT setup provided at a rate of 1 kHz. The lower sampling rate causes an increase of the effective measurement delay of 450 μs in the loop transfer function. The system was otherwise left unchanged; no control-gains were adapted. Figure 11 illustrates the setup of the experiment. The digital real-time control system in use at TCV [62] allowed quick employment of the signals provided by the RT-OFIT setup.

To stabilize an unstable system using feedback control, the bandwidth f_{bw} of the control system must be higher than the frequency (1/growth rate) of the instability. At this bandwidth f_{bw} the phase lag of the open loop transfer function must not exceed 180 degrees to provide a negative, suppressing feedback to the instability. The total phase lag of the open loop transfer function also contains significant contributions of controller implementation and plant dynamics, and should allow robustness margins. This imposes requirements on the response time of the measurement, as at a frequency f every time delay Δt in the feedback loop adds a phase lag $\Delta\phi$ of

$$\Delta\phi = \Delta t \cdot f \cdot 360. \tag{5.3}$$

The reduced growth rates of the vertical instability of the plasmas used for this feedback control experiment are approximately 50-100 Hz, estimated on the basis of a vertical displacement event that occurred where the vertical position signal was lost. The total delay of the loop transfer function at a bandwidth of $f_{bw} > 100$ Hz must therefore be well below 5 ms. The measured processing time in the RT-OFIT setup between the end of the camera exposure and the finished reconstruction output was 1.05 ms. With camera image exposure times of up to 1 ms, and usually around 0.5 ms, and a sampling contribution of $1/2f_s$=0.5 ms, this results in an effective measurement delay of approximately 2 ms.

The magnetic vertical position Z observer is a function of the location and distribution of the plasma current, as opposed to the location of the plasma lower boundary as measured with RT-OFIT. For a constant plasma shape and current distribution however, identical displacements are expected for the

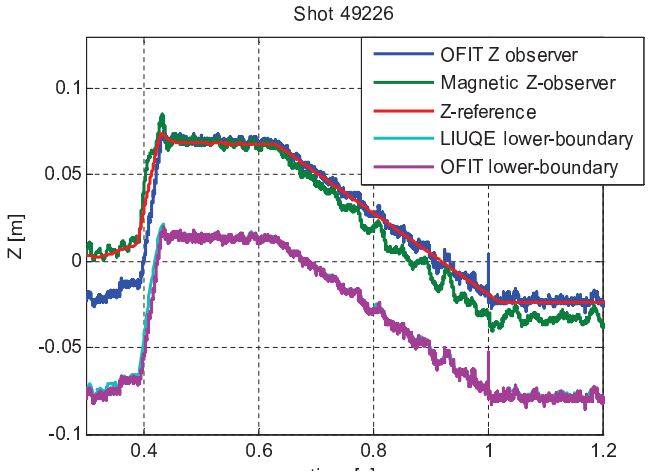

Figure 5.12: Vision-in-the-loop experiment demonstrating vertical position control using RT-OFIT.

Z-observer and the plasma boundary. In the RT-OFIT feedback experiment, the vertical displacement of the plasma boundary is used as a measure of the displacement of the plasma vertical position Z. To ensure continuity in the vertical position signal, the difference between the OFIT lower-boundary and the magnetic Z-observation is sampled at the start of the RT-OFIT control interval. This offset is added as a constant to the OFIT lower-boundary measurement measurement during the RT-OFIT control interval. This ensures continuity in the vertical-position signal for control, and results in an experiment where the vertical position of the plasma with respect to its initial position at the start of flattop is feedback controlled using the RT-OFIT lower-boundary measurement. The vertical position of the boundary at a radius of 0.9 m is used.

For the feedback control experiments, a standard-like plasma shape was adopted. During the current flattop of the discharge, a 9 cm scan of the vertical position of the plasma was programmed to test the tracking performance of the vision-in-the-loop system. The start-up phase of the shot was handled by the existing magnetic measurement and control system. Shortly after the start of flattop, the Z-observer signal normally measured using magnetic pick-up coils is substituted by the Z-measurement of the RT-OFIT system. In this initial implementation, the rest of the feedback control loop was left unchanged.

Figure 5.12 shows vertical position signals from TCV shot 49226, in which the RT-OFIT lower-boundary measurement was used for feedback control between t=0.5 s and t=1.2 s. The figure shows the Z-reference, real-time magnetic Z-observer, real-time OFIT Z-observer and lower boundary, and the lower-boundary from post-shot equilibrium reconstruction. The real-time OFIT Z-observer is obtained by adding an offset to the measured lower boundary signal, sampled at t=0.5 s as the different between the magnetic Z-observer and the OFIT lower boundary measurement. Until t=0.5 s, vertical control is based on the magnetic Z-observer, which is tracking the Z-reference (in red). From t=0.5 s, the OFIT Z observer is used for feedback control. The OFIT Zobserver tracks the reference signal with an average tracking error of 0.5 mm and a standard deviation σ=2.3 mm, demonstrating the effectiveness of the control system with vision-in-the-loop.

During the downward scan of the vertical position, a deviation between the OFIT Z-observer and the magnetic Z-observer is apparent, which reaches a magnitude of 1cm at the end of flattop. Figure 5.12 also shows the lower boundary location from post-shot equilibrium reconstruction with the LIUQE code. Analysis of the vertical displacements of all signals reveals that the displacement in the magnetic Z-observer is proportional to the displacement in the magnetic axis location as found by LIUQE, while the displacement in the OFIT Z-observer is proportional to the displacement in the lower-boundary as found by LIUQE. This is consistent with the physics of both measurements, and suggest the plasma shape was not constant during the experiment. The average difference between the OFIT lower-boundary and LIUQE lower-boundary measurement is 1.1 mm, with a standard deviation σ=1.7 mm.

The vertical position control experiment was reproduced with varying values of elongation, and therefore varying vertical instability growth rates, with similar results. The real-time optical measurement of the plasma position was crucial to both tracking and stabilization of the plasma vertical position. This was demonstrated in an experiment where the optical boundary signal was cut off during the vision-in-

the-loop interval. Within 10 ms a vertical displacement event resulting in a vertical excursion terminated the plasma discharge.

5.6 Conclusions and outlook

This paper describes the design, implementation and usage of a dual real-time camera diagnostic for realtime plasma boundary reconstruction. Example plasma boundary reconstructions were shown and a feedback control experiment using the new diagnostic was presented, demonstrating the application of OFIT in a realtime control environment. Optically reconstructed plasma boundaries show agreement with equilibrium reconstruction results to within 1 cm. The delay in the reconstruction of the measurement between the closing of the camera shutter and the reconstruction output is measured to be 1050 μs. In plasma vertical position control experiments, the real-time functionality of the RT-OFIT system was demonstrated by providing stabilization of the reduced vertical growth rate and tracking of a reference signal. The real-time measurement of segments of plasma boundary is ideally suited to gap-control applications, and could additionally be used to constrain real-time or post-shot magnetic reconstruction codes by providing an absolute measurement of the plasma boundary, making it especially relevant to long discharges.

Visible light emission of the plasma boundary in the TCV tokamak was observed to show significant poloidal inhomogeneity, inhibiting the optical reconstruction of parts of the plasma boundary. Further research is needed to gain full understanding of the causes for these emission profiles.

The use of a narrowband optical filter to acquire images of the C-III emission line was demonstrated. Similar to the broadband visible images, the C-III images also showed localized boundary features. However, the emissive region was narrower than in broadband visible light images, and resulted in reduced noise in the reconstruction of the plasma boundary. Additionally, fewer reflections from vessel structures were visible, further reducing unwanted disturbances in the camera images. Depending on the impurities present in tokamaks, the radial location and width of the emission profile for different impurities may vary. These results extend the application range of the diagnostic to tokamaks where deuterium-Alpha emission from the boundary may not be available, provided a suitably radiating confined impurity is present. In case of multiple such radiating species, the spatial distribution of radiation at various wavelengths can be imaged simultaneously and related to the plasma configuration.

The real-time imaging, acquisition and processing hardware of the RT-OFIT diagnostic can find numerous other applications besides plasma boundary reconstruction by adapting the image processing, optics and number of cameras. A real-time observer of the plasma break-down to provide an estimate of the filament location and size can be used for doublet breakdown control or in large machines where magnetic accuracy during breakdown is lacking. Additionally, multi-camera spectroscopic diagnostics can be conceived to monitor different emission lines along the same lines of sight, with applications such as divertor detachment and impurity seeding penetration monitoring, providing real-time sensors for control of detachment and radiation fraction.

Bibliography

[1] R A Berner. The long-term carbon cycle, fossil fuels and atmospheric composition. *Nature*, 426:323–326, 2003.

[2] Intergovernmental Panel on Climate Change. *Fourth Assessment Report: Climate Change 2007: The AR4 Synthesis Report*. Geneva: IPCC, 2007.

[3] D J C Mackay. *Sustainable Energy without the hot air* . UIT Cambridge Ltd., 2008.

[4] J R Parkins and R Haluza-delay. Social and Ethical Considerations of Nuclear Power Development. *Staff Paper Series*, pages 1–39, 2011.

[5] J Wesson and D J Campbell. *Tokamaks*. International Series of Monographs on Physics. OUP Oxford, 2011.

[6] W M Stacey. *Fusion Plasma Physics*. Physics textbook. Wiley, 2008.

[7] Joint European Torus. http://www.efda.org/jet/.

[8] Mega-Ampere Spherical Tokamak. http://www.ccfe.ac.uk/MAST.aspx.

[9] F. Hofmann, J. B. Lister, W. Anton, S. Barry, R. Behn, S. Bernel, G Besson, F Buhlmann, R Chavan, M Corboz, M J Dutch, B P Duval, D Fasel, A Favre, S Franke, A Heym, A Hirt, C Hollenstein, P Isoz, B Joye, X Llobet, J C Magnin, B Marletaz, P Marmillod, Y Martin, J M Mayor, J M Moret, C Nieswand, P J Paris, A Perez, Z A Pietrzyk, R A Pitts, A Pochelon, R Rage, O Sauter, G Tonetti, M Q Tran, F Troyon, D J Ward, and H Weisen. Creation and control of variably shaped plasmas in tcv. *Plasma Physics and Controlled Fusion*, 36(12B):B277, 1994.

[10] R Aymar, P Barabaschi, and Y Shimomura. The ITER design. *Plasma Physics and Controlled Fusion*, 44:519–565, 2002.

[11] V S Mukhovatov and V D Shafranov. Plasma equilibrium in a tokamak. *Nuclear Fusion*, 11(6):605, 1971.

[12] A Loarte. Effects of divertor geometry on tokamak plasmas. *Plasma Physics and Controlled Fusion*, 43:R183–R224, 2001.

[13] J M Moret, M Anton, S Barry, R Behn, G Besson, F Buhlmann, A Burri, R Chavan, M Corboz, C Deschenaux, M J Dutch, B P Duval, D Fasel, A Favre, S Franke, A Hirt, F Hofmann, C Hollenstein, P F Isoz, B Joye, J B Lister, X Llobet, J C Magnin, P Mandrin, B Marletaz, P Marmillod, Y Martin, J M Mayor, J Moravec, C Nieswand, P J Paris, A Perez, Z A Pietrzyk, V Piffl, R A Pitts, A Pochelon, O Sauter, W van Toledo, G Tonetti, M Q Tran, F Troyon, D J Ward, and H Weisen. Ohmic h-mode and confinement in tcv. *Plasma Physics and Controlled Fusion*, 37(11A):A215, 1995.

[14] F Crisanti, P J Lomas, O Tudisco, A Bcoulet, M Bcoulet, L Bertalot, T Bolzonella, G Bracco, M De Benedetti, B Esposito, C Giroud, N C Hawkes, T C Hender, O N Jarvis, E Joffrin, D Pacella, V Riccardo, F Rimini, K D Zastrow, and contributors to the EFDA-JET Workprogramme. Role of the plasma shaping in itb experiments on jet. *Plasma Physics and Controlled Fusion*, 45(4):379, 2003.

[15] A Beghi and A Cenedese. Advances in real-time plasma boundary reconstruction: from gaps to snakes. *Control Systems, IEEE*, 25, 2005.

[16] M Ariola and A Pironti. *Magnetic Control of Tokamak Plasmas*. Advances in industrial control. Springer, 2008.

[17] I H Hutchinson. *Principles of Plasma Diagnostics: Second Edition*, volume 44. 2002.

[18] A J H Donné, A E Costley, and A W Morris. Diagnostics for plasma control on demo: challenges of implementation. *Nuclear Fusion*, 52(7):074015, 2012.

[19] D P O'Brien, L L Lao, E R Solano, M Garribba, T S Taylor, J G Cordey, and J J Ellis. Equilibrium analysis of iron core tokamaks using a full domain method. *Nuclear Fusion*, 32:1351–1360, 1992.

[20] D Testa, M Toussaint, R Chavan, J Guterl, J B Lister, J-M Moret, A Perez, F Sanchez, B. Schaller, G. Tonetti, A. Encheva, G. Vayakis, C. Walker, Y. Fournier, T. Maeder, A. Le-Luyer, P. Moreau, G. Chitarin, E. Alessi, R.S. Delogu, A. Gallo, N. Marconato, S. Peruzzo, M. Preindl, H. Carfantan, E. Hodgson, J. Romero, R. Vila, B. Brichard, and L. Vermeeren. The Magnetic Diagnostic Set for ITER. *IEEE Transactions on Plasma Science*, 38(3):284–294, March 2010.

[21] J Santos, L Guimarãis, M Zilker, W Treutterer, and M Manso. Reflectometry-based plasma position feedback control demonstration at ASDEX Upgrade. 52:032003, 2012.

[22] J Storrs, J Dowling, G Counsell, and G McArdle. Real-time optical plasma edge detection and position control on MAST. *Fusion Engineering and Design*, 81(15-17):1841–1845, July 2006.

[23] G Hommen, M de Baar, P Nuij, G McArdle, R Akers, and M Steinbuch. Optical boundary reconstruction of tokamak plasmas for feedback control of plasma position and shape. *Review of Scientific Instruments*, 81(11):113504, 2010.

[24] G Hommen, M de Baar, B P Duval, Y Andrebe, H B Le, M A Klop, N J Doelman, G Witvoet, M Steinbuch, and the TCV Team. Real-time optical plasma boundary reconstruction for plasma position control at the tcv tokamak. *Nuclear Fusion*, 54(7):073018, 2014.

[25] G Hommen, M de Baar, J Citrin, H J de Blank, R J Voorhoeve, M F M de Bock, M Steinbuch, and JET-EFDA contributors. A fast, magnetics-free flux surface estimation and q -profile reconstruction algorithm for feedback control of plasma profiles. *Plasma Physics and Controlled Fusion*, 55(2):025007, 2013.

[26] T S Taylor, H St John, A D Turnbull, V R Lin-Liu, K H Burrell, V Chan, M S Chu, J R Ferron, L L Lao, R J La Haye, E A Lazarus, R L Miller, P A Politzer, D P Schissel, and E J Strait. Optimized profiles for improved confinement and stability in the diii-d tokamak. *Plasma Physics and Controlled Fusion*, 36(12B):B229, 1994.

[27] A C C Sips, for the Steady State Operation, and the Transport Physics topical groups of the International Tokamak Physics Activity. Advanced scenarios for iter operation. *Plasma Physics and Controlled Fusion*, 47(5A):A19, 2005.

[28] H Weisen, Y Martin, J-M Moret, and Tcv Team. On the dependence of energy confinement on elongation in single null divertor plasmas. *Nuclear Fusion*, 42(4):L5–L7, April 2002.

[29] W Suttrop, O Gruber, B Kurzan, H D Murmann, J Neuhauser, J Schweinzer, J Stober, W Treutterer, and the ASDEX Upgrade Team. Effect of plasma shape variation on elms and h-mode pedestal properties in asdex upgrade. *Plasma Physics and Controlled Fusion*, 42(5A):A97, 2000.

[30] L Jia-rong. Review of the equilibrium fitting for non-circular tokamak. *Plasma Science and Technology*, 4(2):1183, 2002.

[31] Ph Moreau, F Saint-Laurent, and J B Lister. Drift-free magnetic equilibrium reconstruction using the response to plasma position modulation. *Fusion Engineering and Design*, 84:1339–1343, 2009.

[32] R Albanese, G Artaserse, and M Mattei. Plasma reconstruction in tokamaks with linearized approaches. *Int. J. Appl. Electromagn. Mech.. . .*, 26:191–199, 2007.

[33] A Kirk, N Ben Ayed, G Counsell, B Dudson, T Eich, A Herrmann, B Koch, R Martin, A Meakins, S Saarelma, R Scannell, S Tallents, M Walsh, H R Wilson, and the MAST team. Filament structures at the plasma edge on mast. *Plasma Physics and Controlled Fusion*, 48(12B):B433, 2006.

[34] F S Zaitsev R J Akers L C Appel D Taylor D P Kostomarov, A A Lukianitsa and V V Zlobin. *Proceedings of the 32nd EPS Conference on Plasma Physics, Tarragona, Spain, 27 June1 July 2005*, 29C.

[35] Tore Supra tokamak. http://www-fusion-magnetique.cea.fr/gb/cea/ts/ts.htm.

[36] Photron high-speed cameras. http://www.photron.com/.

[37] J. Storrs. Private communications.

[38] M Groth, G D Porter, T W Petrie, M E Fenstermacher, and N H Brooks. Investigation of main-chamber and divertor recycling in diii-d using tangentially viewing cid cameras. In *Proceedings of the 30th EPS Conference on Controlled Fusion and Plasma Physics, St. Petersburg, Russia, Jul 07 - Jul 11, 2003*.

[39] Vision Research high-speed cameras. http://www.visionresearch.com/.

[40] C E Kessel and N L Bretz. Plasma boundary reconstruction from reflectometer arrays. *Nuclear Fusion*, 39(4):445, 1999.

[41] H Murmann and M Huang. Thomson scattering diagnostic in the boundary layer of asdex. *Plasma Physics and Controlled Fusion*, 27(2):103, 1985.

[42] R J Voorhoeve. Validation of the ofit technique for the detection of the plasma boundary at mast. Eindhoven University of Technology, Control Systems Technology report CST 2011.037, 2011.

[43] R Scannell, M J Walsh, P G Carolan, A C Darke, M R Dunstan, R B Huxford, G McArdle, D Morgan, G Naylor, T O'Gorman, S Shibaev, N Barratt, K J Gibson, G J Tallents, and H R Wilson. Design of a new Nd:YAG Thomson scattering system for MAST. *The Review of scientific instruments*, 79:10E730, 2008.

[44] N J Conway, M F M De Bock, C A Michael, M J Walsh, P G Carolan, N C Hawkes, E Rachlew, J F G McCone, S Shibaev, and G Wearing. The MAST motional Stark effect diagnostic. *The Review of scientific instruments*, 81:10D738, 2010.

[45] G S Lee, J Kim, S M Hwang, C S Chang, H Y Chang, M H Cho, B H Choi, K Kim, K W Cho, S Cho, K K Choh, C.H. Choi, J.H. Choi, J.W. Choi, I.S. Choi, C.J. Do, T.H. Ha, J.H. Han, J.S. Hong, K.H. Hong, N.I. Hur, I.S. Hwang, K.H. Im, H.G. Jhang, Y.S. Jung, B.C. Kim, D.L. Kim, G.H. Kim, H.S. Kim, J.S. Kim, J.Y. Kim, W.C. Kim, Y.S. Kim, K.H. Kwon, M.C. Kyum, B.J. Lee, D.K. Lee, H.G. Lee, J.M. Lee, S.G. Lee, H.G. Na, Y.K. Oh, J.H. Park, H.C. Ri, Y.S. Ryoo, K.Y. Song, H.L. Yang, J.G. Yang, B.J. Yoo, S.J. Yoo, N.S. Yoon, S.B. Yoon, G.H. You, K.I. You, W. Choe, D.-I. Choi, S.G. Jeong, D.Y. Lee, Y.S. Bae, H.S. Kang, G.N. Kim, I.S. Ko, W. Namkung, J.S. Oh, Y.D. Bae, Y.S. Cho, B.G. Hong, G. Hong, C.K. Hwang, S.R. In, M.H. Ju, H.J. Lee, B.H. Oh, B.J. Yoon, S. Baang, H.J. Choi, J. Hwang, M.G. Kim, Y.J. Kim, S.I. Lee, J. Yee, C.S. Yoon, K.-H. Chung, S.H. Hong, Y.S. Hwang, S.H. Kim, Y.H. Kim, K.H. Chung, J.Y. Lim, D.W. Ha, S.S. Oh, K.S. Ryu, Q.L. Wang, T.K. Ko, J. Joo, S. Suh, C.H. Choi, J.H. Lee, Y.W. Lee, H.S. Shin, I.H. Song, J. Baek, I.Y. Han, Y. Koh, P.Y. Park, C. Ryu, J.J. Cho, D.M. Hwang, Y.S. Kim, J.A. Schmidt, H.K. Park, G.H. Neilson, W.T. Reiersen, R.T. Simmons, S. Bernabei, F. Dahlgren, L.R. Grisham, S.C. Jardin, C.E. Kessel, J. Manickam, S.S. Medley, N. Pomphrey, J.C. Sinnis, T.G. Brown, R.B. White, K.M. Young, J. Schultz, P.W. Wang, L. Sevier, M.D. Carter, P.M. Ryan, D.W. Swain, D.N. Hill, W.M. Nevins, and B.J. Braams. The kstar project: An advanced steady state superconducting tokamak experiment. *Nuclear Fusion*, 40(3Y):575, 2000.

[46] E Joffrin. Advanced tokamak scenario developments for the next step. *Plasma Physics and Controlled Fusion*, 49(12B):B629, 2007.

[47] J R Ferron, ML Walker, L L Lao, H E St John, D A Humphreys, and J A Leuer. Real time equilibrium reconstruction for tokamak discharge control. 38:1055–1066, 1998.

[48] D A Gates, J R Ferron, M Bell, T Gibney, R Johnson, R J Marsala, D Mastrovito, J E Menard, D Mueller, B Penaflor, S A Sabbagh, and T Stevenson. Plasma shape control on the national spherical torus experiment (nstx) using real-time equilibrium reconstruction. *Nuclear Fusion*, 46(1):17, 2006.

[49] J. Snipes. Private communications.

[50] TCV Tokamak. https://crppwww.epfl.ch/crpp_tcv.html.

[51] J Blum, C Boulbe, and B Faugeras. Real-time plasma equilibrium reconstruction in a tokamak. *Journal of Physics: Conference Series*, 135(1):012019, 2008.

[52] W Schneider, P J McCarthy, K Lackner, O Gruber, K Behler, P Martin, and R Merkel. ASDEX Upgrade MHD equilibria reconstruction on distributed workstations. *Fusion Engineering and Design*, 48:127–134, 2000.

[53] Goedbloed J P Huysmans G T A and Kerner W. Helena equilibrium code. In *The CP90 Europhysics Conference on Computational Physics : Amsterdam, the Netherlands, 10 - 13 September 1990 ; [proceedings]*, page p371.

[54] F Hofmann and G Tonetti. Tokamak equilibrium reconstruction using faraday rotation measurements. *Nuclear Fusion*, 28(10):1871, 1988.

[55] Centre de Recherches en Physique des Plasmas (CRPP). http://crpp.epfl.ch/.

[56] G F Franklin, M L Workman, and D Powell. *Digital Control of Dynamic Systems*. Addison-Wesley Longman Publishing Co., Inc., Boston, MA, USA, 3rd edition, 1997.

[57] Silicon Software framegrabbers. http://www.silicon-software.info/.

[58] CameraLink interface. http://www.compumodules.com/pdf/CameraLinkOfficial.pdf.

[59] Thorlabs Components. http://www.thorlabs.com/.

[60] Optronis GmbH. Optronis high-speed cameras. http://www.optronis.com/.

[61] H Weisen, F Hofmann, M J Dutch, Y Martin, A Pochelon, J-M Moret, B P Duval, A Hirt, J B Lister, Ch Nieswand, R A Pitts, Z A Pietrzyk, M Anton, R Behn, G Besson, F Bhlmann, R Chavan, D Fasel, A Favre, S Franke, P Isoz, P Lavanchy, B Joye, X Llobet, P Mandrin, B Marletaz, Ph Marmillod, J C Magnin, J-M Mayor, P J Paris, A Perez, O Sauter, W van Toledo, G Tonetti, M Q Tran, F Troyon, and D J Ward. Ohmic h-modes in the tcv tokamak. *Plasma Physics and Controlled Fusion*, 38(8):1137, 1996.

[62] H B Le, F Felici, J I Paley, B P Duval, J-M Moret, S Coda, O Sauter, D Fasel, and P Marmillod. Distributed digital real-time control system for the tcv tokamak. *Fusion Engineering and Design*, (0):–, 2013.

[63] L L et al Lao. *Fusion Sci. Technol.*, 48:968–977, 2005.

[64] R Giannella, N C Hawkes, R Jayakumar, M Makowski, and L Zabeo. Point-to-point analysis of MSE data for plasma diagnostics and control. *Review of Scientific Instruments*, 75:4247, 2004.

[65] L L Lao. Variational moment solutions to the GradShafranov equation. *Physics of Fluids*, 24:1431, 1981.

[66] B Lloyd, R J Akers, F Alladio, S Allan, L C Appel, M Barnes, N C Barratt, N Ben Ayed, B N Breizman, M Cecconello, C D Challis, I T Chapman, D Ciric, G Colyer, J W Connor, N J Conway, M Cox, S.C. Cowley, G. Cunningham, A. Darke, M. De Bock, E. Delchambre, G. De Temmerman, R.O. Dendy, P. Denner, M.D. Driscoll, B. Dudson, D. Dunai, M. Dunstan, S. Elmore, A.R. Field, G. Fishpool, S. Freethy, L. Garzotti, K.J. Gibson, M.P. Gryaznevich, W. Guttenfelder, J Harrison, R.J. Hastie, N.C. Hawkes, T.C. Hender, B. Hnat, D.F. Howell, M.-D. Hua, A. Hubbard, G. Huysmans, D. Keeling, Y.C. Kim, A. Kirk, Y. Liang, M.K. Lilley, M. Lisak, S. Lisgo, Y.Q. Liu, G.P. Maddison, R. Maingi, S.J. Manhood, R. Martin, G.J. McArdle, J. McCone, H. Meyer, C. Michael, S. Mordijck, T. Morgan, A.W. Morris, D.G. Muir, E. Nardon, G. Naylor, M.R. O'Brien,

T. O'Gorman, J. Plenk, A. Patel, S.D. Pinches, M.N. Price, C.M. Roach, V. Rozhansky, S. Saarelma, S.A. Sabbagh, A. Saveliev, R. Scannell, S.E. Sharapov, V. Shevchenko, S. Shibaev, D. Stork, J. Storrs, W. Suttrop, A. Sykes, P. Tamain, D. Taylor, D. Temple, N. Thomas-Davies, A. Thornton, M.R. Turnyanskiy, M. Valovic, R.G.L. Vann, G. Voss, M.J. Walsh, S.E.V. Warder, H.R. Wilson, M. Windridge, M Wisse, S. Zoletnik, the MAST, and NBI teams. Overview of physics results from mast. *Nuclear Fusion*, 51(9):094013, 2011.

[67] J Pamela, J Ongena, and JET EFDA Contributors. Overview of jet results. *Nuclear Fusion*, 45(10):S63, 2005.

[68] H Takatsu. ITER project and fusion technology. *Nuclear Fusion*, 51:094002, 2011.

[69] J F Artaud, V Basiuk, F Imbeaux, M Schneider, J Garcia, G Giruzzi, P Huynh, T Aniel, F Albajar, J M Ané, A Bécoulet, C Bourdelle, A Casati, L Colas, J Decker, R Dumont, L G Eriksson, X Garbet, R Guirlet, P Hertout, G.T. Hoang, W. Houlberg, G. Huysmans, E. Joffrin, S.H. Kim, F. Köchl, J. Lister, X. Litaudon, P. Maget, R. Masset, B. Pégourié, Y. Peysson, P. Thomas, E. Tsitrone, and F. Turco. The CRONOS suite of codes for integrated tokamak modelling, 2010.

[70] J Citrin, J F Artaud, J Garcia, G M D Hogeweij, and F Imbeaux. Impact of heating and current drive mix on the iter hybrid scenario. *Nuclear Fusion*, 50(11):115007, 2010.

[71] B A Hennen, E Westerhof, P W J M Nuij, J W Oosterbeek, M R de Baar, W A Bongers, A Brger, D J Thoen, M Steinbuch, and the TEXTOR Team. Real-time control of tearing modes using a line-of-sight electron cyclotron emission diagnostic. *Plasma Physics and Controlled Fusion*, 52(10):104006, 2010.

[72] F Volpe, M E Austin, G Campbell, and T Deterly. Oblique electron-cyclotron-emission radial and phase detector of rotating magnetic islands applied to alignment and modulation of electron-cyclotron-current-drive for neoclassical tearing mode stabilization. *Review of Scientific Instruments*, 83(10):–, 2012.

[73] L Cheng, M Gong, D Schuurmans, and T Caelli. Real-time discriminative background subtraction. *Image Processing, IEEE Transactions on*, 20(5):1401–1414, May 2011.

[74] J M McHugh, J Konrad, V Saligrama, and P Jodoin. Foreground-adaptive background subtraction. *Signal Processing Letters, IEEE*, 16(5):390–393, May 2009.

[75] D C Brown. *Photogramm. Eng.*, 7:444.